The contribution of semi-arid ecosystems to interannual global carbon cycle variability

Benjamin Poulter[1,2], David Frank[3], Philippe Ciais[2], Ranga Myneni[4], Niels Andela[5], Jian Bi[4], Gregoire Broquet[2], Josep G. Canadell[6], Frederic Chevallier[2], Yi Y. Liu[7], Steven W. Running[8], Stephen Sitch[9], and Guido R. van der Werf[5]

[1] *Montana State University, Institute on Ecosystems and the Department of Ecology, Bozeman, MT 59717, USA*
[2] *Laboratoire des Sciences du Climat et de l'Environnement, LSCE CEA CNRS UVSQ, 91191 Gif Sur Yvette, France*
[3] *Swiss Federal Research Institute WSL, Dendroclimatology, Zürcherstrasse 111, Birmensdorf 8903, Switzerland and Oeschger Centre for Climate Change Research, University of Bern, Bern, Switzerland*
[4] *Department of Earth and Environment, Boston University, 685 Commonwealth Avenue, Boston, MA 02215, USA*
[5] *Faculty of Earth and Life Sciences, VU University, Amsterdam, The Netherlands*
[6] *Global Carbon Project, CSIRO Marine and Atmospheric Research, Canberra, ACT 2601, Australia*
[7] *Water Research Centre, School of Civil and Environmental Engineering, University of New South Wales, Sydney, NSW 2052, Australia*
[8] *Department of Ecosystem and Conservation Sciences, University of Montana, Missoula, MT 59812, USA*
[9] *College of Engineering, Computing and Mathematics, University of Exeter, Exeter EX4 4QF, UK*

¶ Corresponding Author Email: benjamin.poulter@montana.edu

Revised version March 27, 2014

The land and ocean act as a sink for fossil fuel emissions thereby slowing the rise of atmospheric carbon dioxide concentrations[1]. While the uptake of carbon by oceanic and terrestrial processes has kept pace with accelerating carbon dioxide emissions to date, atmospheric carbon dioxide

concentrations exhibit a large variability on interannual timescales[2], considered to be driven primarily by terrestrial ecosystem processes dominated by tropical rainforests[3]. Here we use a terrestrial biogeochemical model, atmospheric inversion and global carbon budget accounting methods to investigate the evolution of the terrestrial carbon sink over the past 30 years with a focus on the underlying mechanisms responsible for the exceptionally large land carbon sink reported in 2011[2]. Our three terrestrial carbon sink estimates are in good agreement and support the finding of a 2011 record land carbon sink. Surprisingly, we find that the global carbon sink anomaly was driven by semi-arid vegetation activity in the Southern Hemisphere, with almost 60 percent of carbon uptake attributed to Australian ecosystems, where prevalent La Niña conditions caused up to six consecutive seasons of increased precipitation. In addition, since 1981, a six percent expansion of vegetation cover over Australia was associated with a four-fold increase in the sensitivity of continental net carbon uptake to precipitation. Our findings suggest that the higher-turnover rates of carbon pools in semi-arid biomes are an increasingly important driver of global carbon cycle inter-annual variability and that tropical rainforests may become less of a relevant driver in the future. More research is needed to identify to what extent the carbon stocks accumulated during wet years are vulnerable to rapid decomposition or loss through fire in subsequent years.

Each year on average, land and ocean carbon sinks absorb the equivalent of about half of global fossil fuel emissions, thereby providing a critical service that slows the rise in atmospheric CO_2 concentrations[1]. Emissions from fossil fuels and land-use change now surpass 10 billion tons or Petagrams (Pg) of carbon per year, tracking the most carbon intense emission scenarios of the Intergovernmental Panel on Climate Change[4]. Even with this acceleration, the fraction of anthropogenic emissions that accumulates in the atmosphere, the airborne fraction, has remained largely unchanged since 1959 at 44%[2] (p=0.36 for slope of linear regression). This implies that the uptake of carbon by ocean and terrestrial processes has, to some extent, kept pace with accelerating emissions due to a range of possible factors, such as the fertilization effect of increased CO_2 and atmospheric nitrogen deposition on plant growth, changes in growing season length, and land management[5]. Associated with the continued uptake of CO_2, the airborne fraction exhibits large variability on interannual timescales, ranging between 18-79% during the past 54 years[2]. This high interannual variability is primarily driven by terrestrial processes which must be better understood to forecast long-term biospheric responses to climate change[3].

Owing to high uncertainties in quantifying ecosystem processes, the global terrestrial carbon sink is often estimated as the residual between emissions from the combustion of fossil fuels, cement production, and net land-use change, and sinks combining accumulation in the atmosphere and uptake by the ocean[6]. Based on this method, the Global Carbon Project reported in their annual assessment a 2011 residual land sink of 4.1±0.9 PgC yr^{-1} (± standard deviation) representing an unusually large increase compared with the 2.6±0.8 PgC yr^{-1} decadal average and the largest reported residual land carbon sink since measurements of atmospheric CO_2 began in 1958. The 2011 residual land sink is indicative of several aspects of the debate surrounding the fate of terrestrial ecosystems under environmental change. First, the large uptake of carbon in

2011 continues a trend of increasing strength in the land carbon sink over at least one decade[1,7]. Second, the large annual growth anomaly in the land carbon sink raises questions regarding the growth rate of atmospheric CO_2 in coming years and how this is affected by the allocation of sequestered carbon to either labile or more stable pools. Lastly, increasing uncertainty in other terms of the global CO_2 budget has direct consequences on land sink estimates, e.g., an overestimate of anthropogenic emissions would be assigned (due to mass conservation and current accounting schemes) as an erroneously large land sink. Thus, attributing changes in net carbon uptake to carbon cycle processes requires a range of methodological approaches.

Here, we investigate the evolution of the terrestrial carbon sink over the last 30 years and the underlying mechanisms of the exceptionally large 2011 residual land carbon sink in a long-term context using i) a "bottom-up" process-oriented terrestrial biosphere model, ii) a "top-down" atmospheric CO_2 inversion, and iii) satellite observations of photosynthetic activity and vegetation structure. We allocate net land carbon uptake amongst specific geographic regions and provide a mechanistic explanation for the climatic and CO_2 response of net primary production (NPP), heterotrophic respiration (R_h), and disturbance that sum up to define net ecosystem exchange (NEE).

We find high agreement among the three different terrestrial carbon sink estimates that robustly support record 2011 land carbon uptake (Fig. 1a; with uncertainty presented as ±1 standard deviation). The LPJ dynamic global vegetation model (DGVM; ref[8]) estimates a 2011 land sink of 3.9±1.3 PgC yr^{-1}, a 1.3±0.6 PgC yr^{-1} anomaly compared to the 2003-2012 mean sink of 2.6±0.9 PgC yr^{-1} (Fig. 1a and

Extended Data Table 1). Our atmospheric inversion (MACC-II; ref.[9]) yields a 3.7±0.4 PgC yr^{-1} 2011 land sink, equivalent to a 1.0 PgC yr^{-1} anomaly above the 2.7±0.4 PgC yr^{-1} inversion average for 2003-2012. The 2011 land sink estimates by the LPJ DGVM and MACC II inversion were greater than the 97.5th percentile over the period 1981-2012 suggesting a convergence of particularly novel ecosystem and climate states.

Both the atmospheric inversion and DGVM model demonstrate an increased contribution from Southern Hemisphere ecosystems to global net carbon uptake beginning in 2011 (Fig. 1b). These patterns are supported by a large observed positive anomaly in the 2010–2011 inter-hemispheric CO_2 concentration gradient between Mauna Loa (MLO, 19°N) and the Cape Grim (CGO, 40°S) monitoring stations[10]. An increase in global net primary production (NPP) appears to be the main driving mechanism behind the 2011 land sink. Global NPP anomalies within the range of 1.7 PgC simulated from the LPJ model forced with climatic data from CRU TS3.21[11] and 1.6 PgC by the Moderate Resolution Imaging Spectroradiometer (MODIS) NPP algorithm (Fig. 2a), using NCEP-Reanalysis climate data and a light use-efficiency model[12] provide parallel support for this conclusion. Further investigation shows 79% (MODIS) to 87% (LPJ) of the global net primary production anomaly is explained by just 3 semi-arid regions, Australia (AUST), Temperate South America (SAmTe) and Southern Africa (SAf), where ecosystem respiration tends to lag productivity, inducing large net carbon uptake (Fig. 2b, and Extended Data Fig. 1 for regions)[13-15]. In Australia, for example, compared with the 2003-2012 average, LPJ simulated a 45% increase in NPP for 2011, from an average of 1.75 to 2.54 PgC yr^{-1}, but only a 9% increase in R_h (from 1.48 to 1.61 PgC yr^{-1}). Moreover, wetter conditions decreased modeled fire-emissions by 29% (from 0.13 to 0.09 PgC yr^{-1}) yielding a net 0.84 PgC 2011 sink. Similarly, we find our conclusions for the greater sensitivity of NPP to precipitation, and lags in R_h, extend to SAfr and SAmTe. In fact, 51% of the global 2011-net carbon sink was attributed to the three Southern Hemisphere semi-arid regions (Extended Data Table 2), while Australia alone contributed to 57% of the total global LPJ-NEE anomaly.

In addition to MODIS, the AVHRR-FPAR3g satellite product (ref.[16]) provides a long-term record of space-borne observations of the fraction of photosynthetic active radiation. Vegetation greening was widespread globally in 2011, with Austral winter (June–August; JJA) FPAR reaching the highest values ever observed in the entire satellite period (1982-2011). In the Southern Hemisphere, record greening (Fig. 1c) centralized over the same three Southern Hemisphere semi-arid regions (AUST, SAmTe and SAf) and was sustained for nine months spanning 2010 to 2011 (December–February, DJF; March–May, MAM; and JJA). Seasonal FPAR increases over Australia ranged from 4.6% in DJF, 8.7% in MAM, to 5.1% in JJA with all anomalies being prominent extremes in the context of an observed 0.8-1.9% interannual variability over the past 30 years. Notably, 46% (34%) of the land area in Australia experienced increases in FPAR in 2011 of more than 2.5 (3.0) standard deviations from normal in MAM, with positive FPAR anomalies first developing in eastern Australia in DJF, extending to all of Australia in MAM, then remaining in northern Australia in JJA (Extended Data Fig. 2).

To identify proximate causes for the role of semi-arid regions in the 2011 global sink, we performed a full set of LPJ factorial model simulations to isolate the temperature, precipitation, cloud cover and CO_2 contribution to NEE (Extended Data Table 1; methods). An additional 'memory' simulation was conducted to evaluate previous-year climate effects that might have contributed to the extraordinary sink in 2011; the 2010 climate was replaced with a near-neutral year (2009) for the El Niño Southern Oscillation (Extended Data Fig. 3). With respect to pre-industrial CO_2 concentrations (287 ppm), the LPJ simulations suggest CO_2-fertilization enhanced the 2011 net carbon uptake by 4.8 PgC. High precipitation during 2010 and 2011 contributed to 0.62 and 0.52 PgC of the global sink, respectively (Fig. 2c), or ~12%, thereby helping to offset land to atmosphere CO_2 fluxes driven by long-term negative temperature (-0.84 PgC) and direct radiative contributions (-0.32 PgC). In addition, 'memory' effects from 2010 added to the 2011 sink, with the largest difference being a threefold increase in tropical South American NEE when using 2009 climate before 2011. The increase in Amazonian NEE in 2011 was mainly due to recovery from the 2010 Amazon drought[17] that caused a reduction in LPJ-NPP and an increase in LPJ-R_h in 2010, leading to reduced short lived litter carbon pools available for respiration and fire in 2011. While 2011 precipitation explained most of the NEE increase in Australia (a 0.56 PgC yr^{-1} contribution), the climate memory effect also explained 0.21 PgC of the 2011 Australian sink because of high precipitation in 2010 that recharged soil moisture and plant carbohydrate reserves to the benefit NPP in 2011. Among an ensemble of climate indices, the Multivariate El Niño Index (MEI; ref. [18]) consistently explained the highest amount of year-to-year variability over Australia for annual carbon uptake ($r=-0.49$, $p<0.01$) and DJF FPAR greening ($r=-0.52$, $p<0.01$) between 1981 and 2011 (Extended Data Figs 4a-d). This extends earlier findings that found Pacific sea surface temperature as a significant predictor of precipitation-driven greening anomalies as far as South Africa and Australia[19,20]. Notably, the 2010/2011

La Niña, i.e., the MEI negative phase, took place over an especially long time period, as observed from multiple satellite, rain gauge and reanalysis data sources (TRMM, CRU and NCEP-DOE; Extended Data Figs 5a-b), and even lowered global sea levels[21], in addition to altering global carbon uptake[12].

Available evidence points toward an enhanced climatic effect of the 2010/2011 La Niña from interactions with long-term semi-arid region greening trends beginning since at least the early 1980s. For example, since 1982, we found an expansion of vegetation across the Australian landscape (p<0.01 for one-sided Kolmogorov-Smirnov test) where land area with FPAR>20% (30%) increased by 5.6% (3.5%) in the MAM growing-season. The greening trend in semi-arid regions has been previously associated with a range of drivers that include altered precipitation frequency and intensity[22], increased water-use efficiency due to elevated CO_2 effects on leaf stomatal conductance[23], and woody-encroachment following land-use and grazing[22,24]. Over this same 1982-2011 time period, we observed a statistically significant increase in the sensitivity of LPJ net carbon uptake (p<0.001) and AVHRR-FPAR3g vegetation activity (p<0.02) to austral-summer precipitation for the Australian continent (Fig. 3a). The observed change in ecosystem sensitivity over Australia meant that an additional 100 mm of growing season (MAM) precipitation led to a four-fold increase in net carbon uptake when comparing sensitivities before (0.2 PgC yr^{-1} per 100mm) or after (0.8 PgC yr^{-1} per 100mm) 1997, the midpoint of current observational records (1982-2011). An independent data-driven model of net ecosystem production[25], which excluded disturbance processes, confirmed the same statistically robust increase over time in carbon uptake per unit precipitation for Australia (Fig. 3b, p<0.001). Long-term observations from passive-microwave vegetation optical depth (VOD)[26] suggest that the enhanced vegetation sensitivity to climate is a result of both increases in grass cover as well as from woody encroachment (Fig. 3c).

The 2011 land carbon sink anomaly indicates a novel climate response of the biosphere where interactions between possibly human-caused extremes in austral-precipitation[27] and changes in land cover[23] are contributing to non-analog ecosystem behavior with global biogeochemical significance. As such, we propose that the current paradigm, whereby tropical rainforest ENSO coupling dominates inter-annual variability of the atmospheric CO_2 growth rate[3,28], may become less relevant in the future. We explored whether such semi-arid carbon-cycle climate sensitivity feedbacks exist among an ensemble of 15 earth system models, contributed to the Coupled Model Intercomparison Project Phase 5 (CMIP5; ref.[29]). In contrast to our observations, we found that for semi-arid regions, modeled carbon-uptake and precipitation sensitivity remains relatively stable from the 1990 to 2090 period for the CMIP5 ensemble (p=0.33, one-sided t-test, Fig. 4). This suggests that processes contributing to the novel ecosystem dynamics identified here may be overlooked in future climate change scenarios. As the dynamics of semi-arid systems, which cover 45% of the earth's land surface, increase in global importance, more research is needed to identify whether enhanced carbon sequestration in wet years is particularly vulnerable to rapid decomposition or loss through fire in subsequent years, and thus largely transitory. Such behavior may already be reflected by a larger than average atmospheric growth rate in 2012[30] that was associated with a return to near-normal terrestrial land sink conditions (Fig. 1a).

Methods Summary

We use multiple data sources, including carbon accounting methods, carbon-cycle model simulations, and satellite-based vegetation products to investigate the magnitude and mechanisms driving variability in the terrestrial carbon sink. Net Primary Production (NPP), or the total photosynthesis minus plant autotrophic respiration losses, is simulated by the LPJ DGVM and also estimated independently with the MODIS NPP algorithm, MOD17A3. The balance between carbon uptake from net primary production and losses from soil respiration and disturbance (i.e., net ecosystem exchange; NEE), is quantified from the Global Carbon Project, the LPJ Dynamic Global Vegetation Model (DGVM), and the MACC-II atmospheric inversion system. Net ecosystem production (NEP), i.e., the balance between gross carbon inputs from photosynthesis and losses from ecosystem respiration, excluding disturbance, is estimated from upscaled FLUXNET observations. Optical and passive microwave satellite data are employed to assess vegetation greenness trends (AVHRR FPAR3g) and vegetation structure or vegetation optical depth (VOD). Monthly and seasonal precipitation fluctuation is quantified from the Tropical Rainfall Measurement Mission (TRMM 3B43v7) and NCEP-DOE Reanalysis II, and the Climatic Research Unit (CRU) TS3.21. Regional summaries of the global gridded data followed boundaries from the eleven TRANSCOM atmospheric inversion land regions. We further differentiate North and South Africa to distinguish between wet and semi-arid climates with the ratio of precipitation (P) to potential evaporation (PET) set to 0.7. Historical (1860-2005) simulations of net biome production (NBP), equivalent to NEE, from the Fifth Coupled Model Intercomparison Project (CMIP5) are merged with the Representative Concentration Pathway 8.5 (RCP8.5) to create temporal composites spanning 1860-2099 for 15 earth system models.

Full Methods and any associated references are available in the online version of the paper at www.nature.com/nature.

1 Ballantyne, A. P., Alden, C. B., Miller, J. B., Tans, P. P. & White, J. W. C. Increase in observed net carbon dioxide uptake by land and oceans during the past 50 years. *Nature* **488**, 70-73 (2012).

2 Le Quéré, C. *et al.* The global carbon budget 1959-2011. *Earth System Science Data* **5**, 1107-1157 (2013).

3 Cox, P. *et al.* Sensitivity of tropical carbon to climate change constrained by carbon dioxide variability. *Nature* **494**, 341-345 (2013).

4 Peters, G. P. *et al.* The challenge to keep global warming below 2 °C. *Nature Climate Change* **3**, 4-6 (2012).

5 Pan, Y. *et al.* A Large and Persistent Carbon Sink in the World's Forests. *Science* **333**, 988-993 (2011).

6 Canadell, J. G. *et al.* Contributions to accelerating atmospheric CO_2 growth from economic activity, carbon intensity, and efficiency of natural sinks. *Proceedings of the National Academy of Science* **104**, 18866-18870 (2007).

7 Sitch, S. *et al.* Trends and drivers of regional sources and sinks of carbon dioxide over the past two decades. *Biogeosci. Disc.* (2013).

8 Sitch, S. *et al.* Evaluation of ecosystem dynamics, plant geography and terrestrial carbon cycling in the LPJ dynamic global vegetation model. *Global Change Biol.* **9**, 161-185 (2003).

9 Chevallier, F. *et al.* CO_2 surface fluxes at grid point scale estimated from a global 21 year reanalysis of atmospheric measurements. *Journal of Geophysical Research: Atmospheres* **115**, D21307, doi:10.1029/2010jd013887 (2010).

10 Francey, R. J. *et al.* Atmospheric verification of anthropogenic CO_2 emission trends. *Nature Climate Change* **3**, 520-524 (2013).

11 Harris, I., Jones, P. D., Osborn, T. J. & Lister, D. H. Updated high-resolution grids of monthly climatic observations – the CRU TS3.10 Dataset. *International Journal of Climatology*, doi:10.1002/joc.3711 (2013).

12 Bastos, A., Running, S. W., Gouveia, C. & Trigo, R. M. The global NPP dependence on ENSO: La-Niña and the extraordinary year of 2011. *Journal of Geophysical Research*, doi: 10.1002/jgrg.20100 (2013).

13 Haverd, V. *et al.* Multiple observation types reduce uncertainty in Australia's terrestrial carbon and water cycles. *Biogeosciences* **10**, 2011-2040 (2013).

14 Haverd, V. *et al.* The Australian terrestrial carbon budget. *Biogeosciences* **10**, 851-869 (2013).

15 Rotenberg, E. & Yakir, D. Contribution of semi-arid forests to the climate system. *Science* **327**, 451-454 (2010).

16 Zhu, Z. *et al.* Global Data Sets of Vegetation LAI3g and FPAR3g derived from GIMMS NDVI3g for the period 1981 to 2011. *Remote Sensing* **5**, 927-948 (2013).

17 Marengo, J. A., Tomasella, J., Alves, L. M., Soares, W. R. & Rodriguez, D. A. The drought of 2010 in the context of historical droughts in the Amazon region. *Geophys. Res. Lett.* **38**, doi:10.1029/2011GL047436 (2011).

18 Wolter, K. & Timlin, M. S. in *Proceedings of the 17th Climate Diagnostics Workshop.* 52-57 (NOAA/NMC/CAC, NSSL).

19 Myneni, R. B., Los, S. O. & Tucker, C. J. Satellite-based identification of linked vegetation index and sea surface temperate anomaly areas from 1982-1990 for Africa, Australia and South America. *Geophys. Res. Lett.* **23**, 729-732 (1996).

20 Woodward, F. I., Lomas, M. R. & Quaife, T. Global responses of terrestrial productivity to contemporary climatic oscillations. *Philos. Trans. R. Soc. Lond., Ser. B: Biol. Sci.* **363**, 2779-2785 (2008).

21 Boening, C., WIllis, J. K., Landerer, F. W., Nerem, R. S. & Fasullo, J. The 2011 La Niña: So strong, the oceans fell. *Geophys. Res. Lett.* **39**, doi:10.1029/2012GL053055 (2012).

22 Donohue, R. J., McVicar, T. R. & Roderick, M. L. Climate-related trends in Australian vegetation cover as inferred from satellite observations, 1981–2006. *Global Change Biol.* **15**, 1025-1039 (2009).

23 Donohue, R. J., Roderick, M. L., McVicar, T. R. & Farquhar, G. D. CO_2 fertilisation has increased maximum foliage cover across the globe's warm, arid environments. *Geophys. Res. Lett.*, doi:10.1002/grl.50563 (2013).

24 Asner, G. P., Elmore, A. J., Olander, L. P., Martin, R. E. & Harris, A. T. Grazing systems, ecosystem responses, and global change. *Annual Review of Environmental Resources* **29**, 261-299 (2004).

25 Jung, M., Reichstein, M. & Bondeau, A. Towards global empirical upscaling of FLUXNET eddy covariance observations: validation of a model tree ensemble approach using a biosphere model. *Biogeosciences* **6**, 5271-5304 (2009).

26 Andela, N., Liu, Y. Y., van Dijk, A. I. J. M., de Jeu, R. A. M. & McVicar, T. R. Global changes in dryland vegetation dynamics (1988–2008) assessed by satellite remote sensing: combining a new passive microwave vegetation density record with reflective greenness data. *Biogeosci. Disc.* **10**, 8749-8797 (2013).

27 Kang, S. M. *et al.* Modeling evidence that ozone depletion has impacted extreme precipitation in the austral summer. *Geophys. Res. Lett.*, doi:10.1002/grl.50769 (2013).

28 Wang, W. *et al.* Variations in Atmospheric CO_2 Growth Rates Controlled by Tropical Temperature. *Proc. Natl. Acad. Sci. USA*, doi:10.1073/pnas.1219683110 (2013).

29 Taylor, K. E., Stouffer, R. J. & Meehl, G. A. An overview of the CMIP5 and the experimental design. *Bulletin of the American Meteorology Society* **93**, 485-498 (2012).

30 Le Quéré, C. *et al.* Global carbon budget 2013. *Earth Syst. Sci. Data Discuss.* **6**, 689-760, doi:10.5194/essdd-6-689-2013 (2013).

31 Chapin, F. S. *et al.* Reconciling Carbon-cycle Concepts, Terminology, and Methods. *Ecosystems* **9**, 1041-1050 (2006).

32 Zaehle, S., Sitch, S., Smith, B. & Hattermann, F. Effects of parameter uncertainty on the modeling of terrestrial biosphere dynamics. *Global*

Biogeochemical Cycles **19**, GB3020, doi:3010.1029/2004GB002395 (2005).

33 Poulter, B., Frank, D., Hodson, E. L., Lischke, H. & Zimmermann, N. E. Impacts of land cover and climate data selection on understanding terrestrial carbon dynamics and the CO_2 airborne fraction. *Biogeosciences* **8**, 2027-2036 (2011).

34 Kaiser, J. W. *et al.* Biomass burning emissions estimated with a global fire assimilation system based on observed fire radiative power. *Biogeosciences* **9**, 527-554 (2012).

35 van der Werf, G. R. *et al.* Global fire emissions and the contribution of deforestation, savanna, forest, agricultural, and peat fires (1997–2009). *Atmospheric Chemistry Physics Discussions* **10**, 16153-16230 (2010).

36 van der Werf, G. R. *et al.* Interannual variability in global biomass burning emissions from 1997-2004. *Atmospheric Chemistry and Physics* **6**, 3423-3441 (2006).

37 Zhao, M. & Running, S. W. Drought-induced reduction in global terrestrial net primary production from 2000 through 2009. *Science* **329**, 940-943 (2010).

38 Moss, R. H. *et al.* The next generation of scenarios for climate change research and assessment. *Nature* **463**, doi:10.1038/nature08823 (2010).

39 Liu, Y. Y., van Dijk, A. I. J. M., McCabe, M. F., Evans, J. P. & de Jeu, R. A. M. Global vegetation biomass change (1988–2008) and attribution to environmental and human drivers. *Global Ecol. Biogeogr.* (2012).

40 Kanamitsu, M. *et al.* NCEP-DEO AMIP-II Reanalysis (R-2). *Bulletin of the American Meteorological Society* **83**, 1631-1643 (2002).

Supplementary Information is linked to the online version of the paper at www.nature.com/nature

Acknowledgements We acknowledge support from the EU FP7 GEOCARBON program, and thank the researchers involved with collecting and maintaining the climate data at the Climate Research Unit, University of East Anglia, UK, and National Center for Atmospheric Research, USA. We also acknowledge the World Climate Research Programme's Working Group on Coupled Modelling, which is responsible for CMIP. We thank the climate modeling groups for producing and making available their model output. For CMIP the U.S. Department of Energy's Program for Climate Model Diagnosis and Intercomparison provides coordinating support and led development of software infrastructure in partnership with the Global

Organization for Earth System Science Portals. We also thank Martin Jung for providing the 'upscaled' NEE data used in our analysis. JGC acknowledges the support of the Australian Climate Change Science Program. Corinne Le Quéré and Lucas Cernusak provided valuable comments and suggestions that improved the manuscript. This paper is a contribution to the Global Carbon Budget activity of the Global Carbon Project.

Author Contributions BP, DF, PC and RM designed the analyses; JB, FC, GB, DF, RM, SWR, SS, GVDW, JGC, YL and NA contributed data to the analyses; BP, FC, RM, SR, and DF conducted the analyses; All authors contributed to the writing of the manuscript.

Author Information Reprints and permissions information is available at www.nature.com/nature. Correspondence and requests for materials should be addressed to benjamin.poulter@montana.edu

Figure 1:

Interannual variability of NEE and FPAR anomalies. (a) Annual NEE, where positive values represent carbon uptake, blue is LPJ, red is MACC-II, and the residual land sink is in grey. The standard deviations are ±0.58 PgC yr^{-1} for LPJ, ±0.4 Pg C yr^{-1} for the inversion, and ±0.8 Pg C yr^{-1} for the residual (see methods), (b) average, 2003-2012, annual NEE for Northern and Southern hemispheres estimated by LPJ and the inversion, and (c) AVHRR FPAR anomalies for the southern (S) and northern (N) hemispheres with respect to the 1982-2011 long-term average where the seasonal anomalies were calculated as the z-score for each season (s) and each grid cell (i,j) for each year (y); $AVHRR_{anomaly,s(i,j)} = \frac{AVHRR_{y,s(i,j)} - AVHRR_{1982-2011,s(i,j)}}{\sigma AVHRR_{1982-2011,s(i,j)}}$.

Figure 2:

Global anomalies of NPP and NEE, and the precipitation effect. (a) Annual NPP anomaly, as z-score (defined in Fig. 1), estimated by the MOD17A3 algorithm that uses MODIS LAI (MOD15 Collection 5)[12]. (b) Annual NEE anomaly, as z-score, estimated by the LPJ-DGVM, where a positive z-score equals larger sink; the reference period is 2000-2011. (c) Spatial pattern of the contribution of precipitation to net ecosystem exchange in 2011 calculated as the difference between NEE with the all climate forcing varied and NEE simulated with the precipitation climatology (see Extended Data Figs 6a-b for NPP and R_h component fluxes).

Figure 3:

Change in climate sensitivity of observations for Australia. (a) Climate sensitivity of annual LPJ-NEE anomalies to March-April-May precipitation anomalies for Australia. The empty circles and/or dashed line are the points and regression line for

1982-1996 (β_1) and the filled circles and solid line for 1997-2011 (β_1+β_3), from the following the linear regression model using NEE and precipitation anomalies (P_{anom}) where A is a 'dummy' variable for the different time periods: ($NEE_{anom} = \beta_0 + \beta_1 P_{anom} + \beta_2 A + \beta_3 P_{anom} A$). (b) Climate sensitivity of annual NEE from the MACC-II inversion (black symbols) and the upscaled NEP product using the same linear model as in Fig. 3a. (c) Climate sensitivity of annual VOD (light green symbols) and Mar-Apr-May FPAR (dark green symbols) also using same model described in Fig. 3a.

Figure 4:

Change in climate sensitivity of CMIP5 models for Australia. Distribution of the change in sensitivity between the 1979-2005 and 2069-2095 in net biome production to annual precipitation for four biomes (*n*=15 CMIP5 earth system models). Precipitation sensitivity was estimated as β_1 while controlling for changes in sensitivity due to CO_2 and temperature $NBP_{anom} = \beta_0 + \beta_1 CO2_{anom} + \beta_2 P_{anom} + \beta_3 Tair_{anom}$. The different lines refer to tropical (green), temperate (brown), semi-arid (tan), and boreal (purple) biomes.

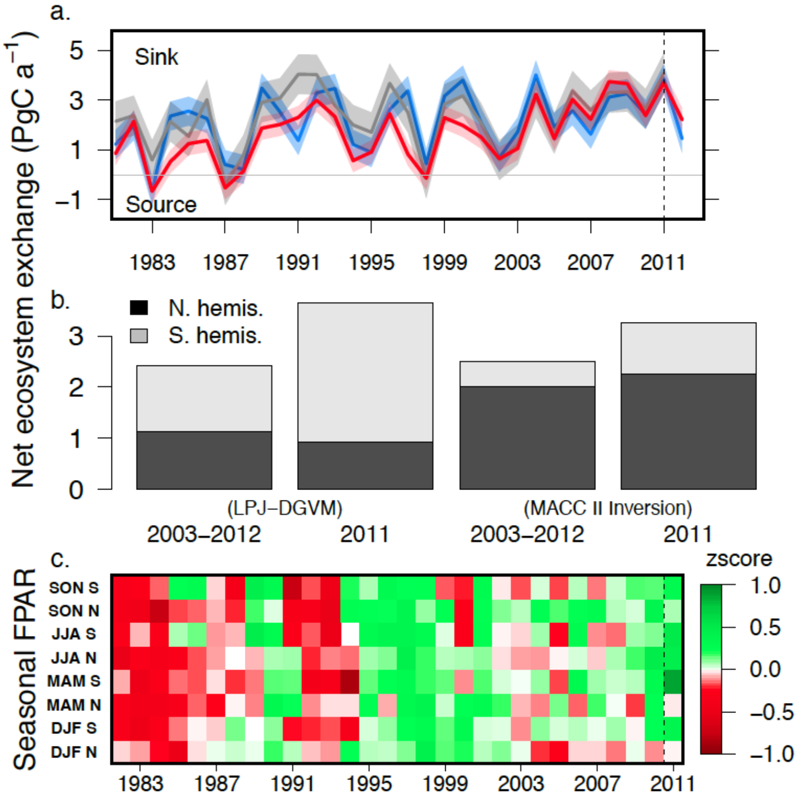

a.
Sink
Source
Net ecosystem exchange (PgC a^{-1})
5
3
1
−1
1983
1987
1991
1995
1999
2003
2007
2011
b.
N. hemis.
S. hemis.
3
2
1
0
(LPJ–DGVM)
(MACC II Inversion)
2003–2012
2011
2003–2012
2011
c.
Seasonal FPAR
SON S
SON N
JJA S
JJA N
MAM S
MAM N
DJF S
DJF N
zscore
1.0
0.5
0.0
−0.5
−1.0
1983
1987
1991
1995
1999
2003
2007
2011

453

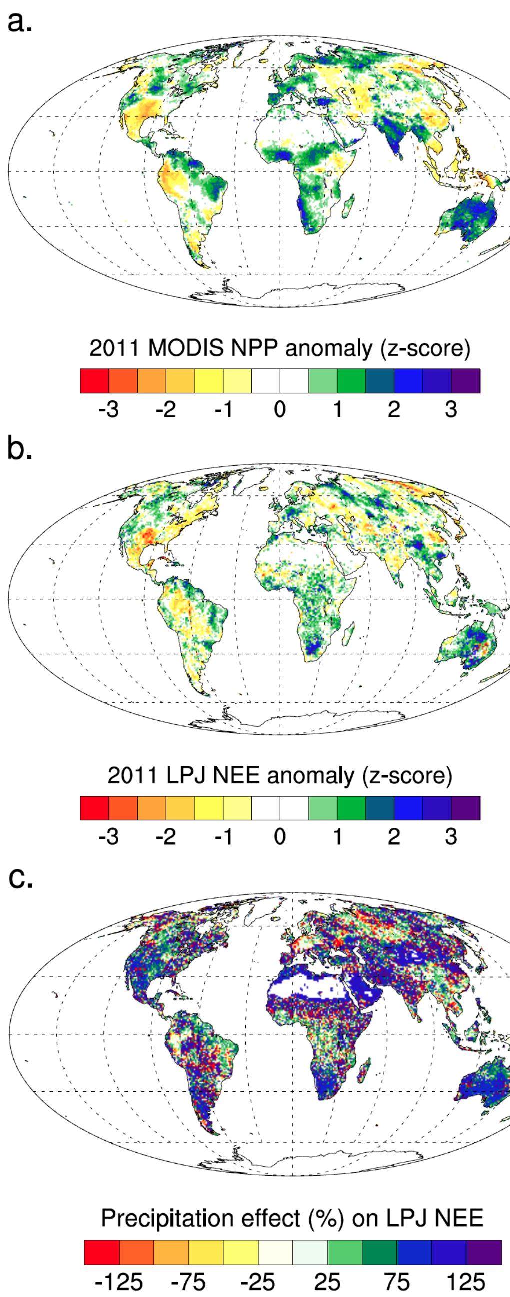
a.
2011 MODIS NPP anomaly (z-score)
-3 -2 -1 0 1 2 3
b.
2011 LPJ NEE anomaly (z-score)
-3 -2 -1 0 1 2 3
c.
Precipitation effect (%) on LPJ NEE
-125 -75 -25 25 75 125

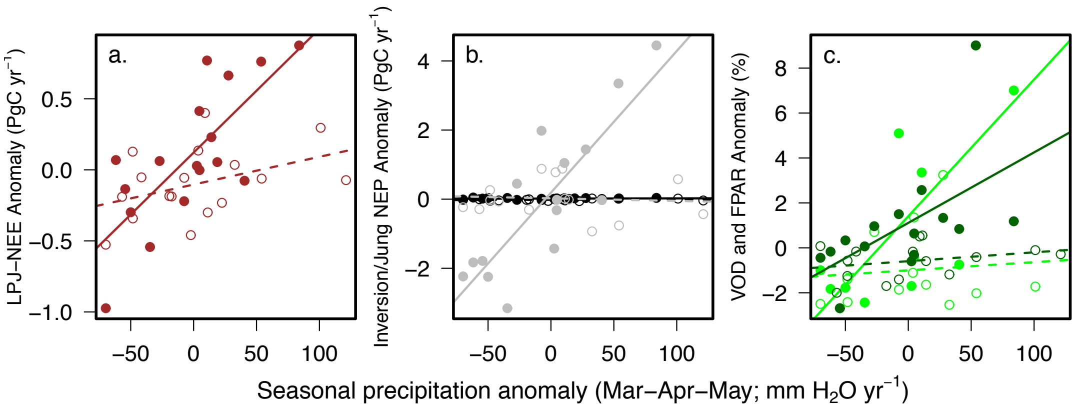
a.
b.
c.
LPJ–NEE Anomaly (PgC yr^{-1})
Inversion/Jung NEP Anomaly (PgC yr^{-1})
VOD and FPAR Anomaly (%)
Seasonal precipitation anomaly (Mar–Apr–May; mm H_2O yr^{-1})

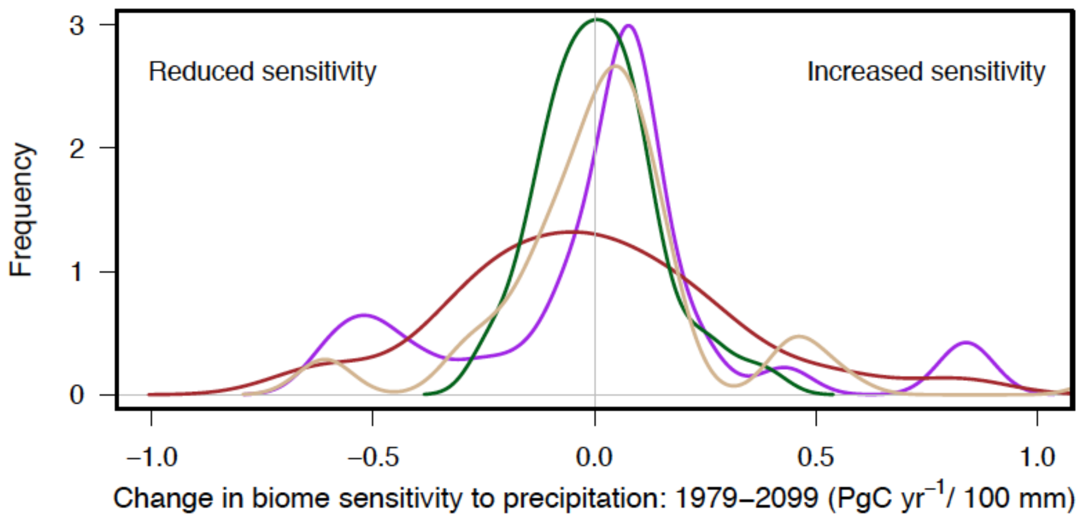
Reduced sensitivity
Increased sensitivity
Frequency
3
2
1
0
−1.0
−0.5
0.0
0.5
1.0
Change in biome sensitivity to precipitation: 1979–2099 (PgC yr−1/ 100 mm)

Methods

Carbon fluxes and their uncertainties: We follow the carbon-cycle definitions summarized by Chapin et al.[31] when describing the net land carbon sink in terms of net ecosystem exchange (NEE) or net ecosystem production (NEP) and associated component fluxes. Data for estimating the airborne fraction, the residual land sink and its anomalies were obtained online from the Global Carbon Project[2] (Version 1.5) for years 1959-2011. Uncertainties are presented as ±1 standard deviation (σ), assuming Gaussian error and a 68% likelihood that the true value is within this range. The LPJ dynamic global vegetation model (DGVM) was run with the GlobFirm fire module enabled and fully prognostic dynamic natural vegetation (excluding land-cover change). The Climatic Research Unit (CRU) TS 3.21 climate dataset[11] was used for LPJ-model simulations starting in 1901 and ending in 2012 with observed rising CO_2 concentrations from ice-core measurement of CO_2 and then the Mauna Loa Observatory after 1958. Uncertainty in LPJ NEE was estimated using a Latin Hypercube (LHC) approach to generate 200 parameter sets and corresponding simulations at 1-degree spatial resolution for 13 of the most important parameters[32]. The observed linear relationship between the LHC model ensemble global mean NEE and its standard deviation (R^2=0.62) was used to predict the 2011 land sink uncertainty for the 0.5-degree simulation and presented as ±1 standard deviation. Uncertainty from climate forcing was considered by comparing different climate datasets (see ***Climate datasets***) and is not likely to affect annual anomalies or trends in carbon fluxes[33]. LPJ simulates semi-arid plant functional types (PFT) by a mix of grasses with C3 and C4 photosynthetic pathways and, in lesser abundance, tropical and temperate trees. Carbon cycle fluxes simulated by LPJ were in close agreement with regionally parameterized models for Australia, such as CABLE[14], and regional

NPP from satellite-based estimates of MODIS (Extended Data Table 2). Simulated losses of carbon from fire and their anomalies were benchmarked with the GFAS v1.0[34] and GFED v3.1[35] datasets that use satellite-observed fire radiative power and burned area, respectively, to estimate carbon emissions (Extended Data Table 3). The atmospheric inversion was based on the MACC-II inversion system version 12.1, described in Chevallier et al.[9], using atmospheric CO_2 data from NOAA/ESRL, WDCGG, CarboEurope and RAMCES, with a climatological prior for NEP land-surface carbon fluxes from the ORCHIDEE DGVM[9] and fire emissions from GFED v3.0[36] until 2011, and the long-term mean substituted for 2012. The inversion is applied on a 3.75x2.5 degree grid with fluxes inverted at weekly resolution and nighttime and daytime fluxes separated. The MACC-II inversion minimizes a Bayesian objective function, assuming errors are Gaussian (posterior errors presented here as ±1 standard deviation), and error correlation implied by off-diagonal elements in the posterior error covariance matrix. Upscaled flux tower observations were the basis for the data-derived NEE model of Jung et al.[25] representing monthly 0.5 degree fluxes from 1982-2011. The MODIS (MOD17A3[37]) product provided annual net primary production data at 1km resolution and was resampled to 8km resolution to match AVHRR-FPAR3g prior to analysis. Net biome production from CMIP5 Representative Concentration Pathway (RCP) 8.5[29,38] ensemble was merged with the corresponding historical simulations to create temporal composites covering years 1860-2099 for 15 earth system models (Extended Data Table 4).

Vegetation activity Measurements of the fraction of photosynthetic active radiation (FPAR) were modeled from surface reflectance observed aboard the Advanced Very High Resolution Radiometer (AVHRR) and incorporated into the FPAR3g[16] dataset (1981 to 2011). The FPAR3g bimonthly dataset was first filtered for low values, within the range of uncertainty (<2.5%), before compositing to monthly values using a maximum values approach. Gridded passive-microwave measurements of Vegetation Optical Depth (VOD) from[39] were aggregated from 0.25 degree resolution to each of the thirteen regional means at a monthly resolution from 1988-2011. The VOD is an indicator of water content in both woody and leaf components of aboveground biomass. The VOD time-series is based on a multi-source dataset consisting of harmonized passive microwave measurements from SSM/I (Special Sensor Microwave Imager, 1988–2007), TMI (the microwave instrument onboard the Tropical Rainfall Measuring Mission satellite, 1998–2008) and AMSR-E (the Advanced Microwave Scanning Radiometer – Earth Observing System, July 2002–08) sensors[39].

Climate datasets Precipitation data from satellite (Tropical Rainfall Measurement Mission, TRMM 3B43v7), reanalysis (NCEP-DOE Reanalysis II[40], 1979-2012), and ground-based observations (CRU TS3.21[11]) were compared with one another for annual and seasonal similarities (Figs Extended Data 5a-b). Over Australia, annual precipitation was observed as up to +205±54 mm (in 2010) and +178±71 mm (in 2011) above the long-term annual average of 555±23 mm yr^{-1}, with uncertainties presented as the standard deviation of the three products. An ensemble of climate indices were evaluated (Figs Extended Data 4a-d) with data for the MEI from Wolter et al.[18], where negative values indicate the La Niña climate mode.

Extended Data

Extended Data Table 1: Global summary of annual net ecosystem exchange (NEE=NPP-RH-FIRE) and its component fluxes estimated from LPJ, the residual, the MACC-II inversion, and from MODIS, GFED, and GFAS. All units are in PgC yr^{-1}.

Extended Data Table 2: Annual LPJ-derived net ecosystem exchange and component flux anomalies (PgC yr^{-1}) for each of the 11 TransCom regions (see Extended Data Fig. 1 for region map). The annual LPJ anomalies for 2011 and 2012 are calculated relative to the 2003 to 2012 time period. MODIS-NPP anomalies, with respect to 2000-2011, are provided in grey text for comparison (but not used in the NEE calculation). A positive NEE anomaly indicates an increase in the carbon sink strength and negative fire anomalies mean a decrease in fire emissions. The total global LPJ NEE anomaly for 2011 was 1.4 PgC yr^{-1}.

Extended Data Table 3: Total carbon emissions from wildfire for each TransCom region estimated from LPJ, GFAS and GFED for the overlapping 2002-2012 averaging period, and for years 2011 and 2012. Units are PgC yr^{-1}.

Extended Data Table 4: CMIP5 Earth system models from PCMDI node 9 that were accessed and where the RCP8.5 scenario (2005-2099) was merged with the historical simulation (1860-2005). Of the total ensemble, 15 models were used in the analysis because a full suite of historical and RCP8.5 simulations were available for the net biome production, air temperature and precipitation variables.

Extended Data Figure 1: The thirteen regions used throughout the analysis, 11 from TRANSCOM, and 2 additional for the African continent to distinguish semi-arid regions (see Methods Summary).

Extended Data Figure 2: Seasonal AVHRR FPAR anomalies (z-score) for year 2011. The z-score is calculated relative to the long term seasonal mean and standard deviation of FPAR (1982-2011), see legend in main text for Fig. 1c. The seasons DJF, MAM, JJA, and SON and defined by the first letter of each month.

Extended Data Figure 3. Full climate attribution of the global land sink simulation by the LPJ DGVM (bars) and the Multivariate El Nino Index (MEI) and Pacific Decadal Oscillation (PDO).

Extended Data Figure 4a-d: Correlation coefficient (r) between climate modes and (a) MAM, and (b) JJA net ecosystem exchange simulated by LPJ for each of the TransCom regions. FPAR correlations between climate modes are shown for (c) MAM and (d) JJA. The correlations were made for 1982-2011. White/blank boxes indicate correlation between -0.1 and 0.1.

Extended Data Figure 5a-b: (a) global temperature and precipitation anomalies from CRU TS 3.2 data. The anomalies are with respect to 1979-2012 seasonal means. **(b)** seasonal precipitation anomalies (z-score) for year 2010 (upper panel) and 2011 (lower panel). The z-score is calculated relative to the long term seasonal mean and standard deviation of precipitation (1979-2011). The seasons DJF, MAM, JJA, and SON and defined by the first letter of each month.

Extended Data Figure 6a-b: Spatial pattern of the contribution of precipitation to net ecosystem exchange in 2011 calculated as the difference between NPP (a) and RH (b) with the all climate forcing varied and NEE simulated with the precipitation climatology. This is the same as in Fig. 2c (main text) but for component fluxes of NEE.